3-D anisotropic elastic ray tracing in smooth media

Ketil Hokstad
Seismics and Formation Physics Department
SINTEF Petroleum Research

Sverre Brandsberg-Dahl
Center for Wave Phenomena
Colorado School of Mines

July 7, 2000

Abstract

A major challenge in prestack Kirchhoff migration in laterally inhomogeneous media is the computation of asymptotic elastodynamic Green's tensor by means of kinetic and dynamic ray tracing. We give a summary of anisotropic elastic ray theory, and describe the numerical implementation of initial ray tracing in 3-D anisotropic elastic media. Moreover, we discuss the interpolation of ray-theoretical quantities which is needed in order to use the ray tracer in a prestack seismic imaging scheme, paying attention to the multipathing, caustics and wavefront triplications that arise in complex media. The numerical ray tracer is designed to be used in seismic imaging and inversion schemes. Therefore only transmitted rays in smooth media are considered.

Contents

1 Introduction **2**

2 Anisotropic elastic ray theory **2**

2.1 Geometrical ray Green's tensor . . . 2

2.2 Christoffel equation . . . 3

2.3 Kinetic ray tracing system . . . 4

2.4 Dynamic ray tracing system . . . 4

2.5 Geometrical spreading . . . 6

3 Numerical ray tracing **6**

3.1 Numerical test model . . . 6

3.2 Initial value ray tracing . . . 7

3.3 Uniform distribution of rays . . . 9

3.4 Interpolation of rays at constant depth . . . 9

3.5 Interpolation of rays on a regular grid . . . 13

3.6 Interpolation of the geological model . . . 14

4 Computational cost **21**

5 Discussion and conclusions **23**

1 Introduction

Asymptotic solutions of the elastodynamic wave equation are important in seismic imaging and inversion in laterally inhomogeneous media. Dynamic ray tracing is needed to perform true-amplitude prestack Kirchhoff migration (Schleicher et al., 1993) and imaging/inversion by means of the generalized Radon transform (GRT) introduced by (Beylkin and Burridge, 1990). Recently, methods based on the geometrical ray approximation (GRA) have been extended to multicomponent data in anisotropic elastic media (Hokstad, 2000), and to account for multipathing in complex structures using the common-angle domain (Xu et al., 1998). de Hoop and Brandsberg-Dahl (1999) developed a Maslov asymptotic extension of GRT imaging to handle multipathing as well as the caustic problems in geometrical ray theory.

The major challenge in implementation of the imaging methods mentioned above is the numerical computation of the asymptotic elastodynamic Green's tensor by kinetic and dynamic ray tracing. We first give a brief summary of ray theory in anisotropic elastic media, following Cerveny (1995). Second, we present in some detail, the numerical implementation of initial-value ray tracing in 3-D anisotropic elastic media. The initial-value ray tracing is performed by fifth-order Runge-Kutta integration of the kinetic and dynamic ray tracing systems. We aslo discuss the subsequent interpolation of ray-theoretical quantities which is required to use the ray-tracer for 3-D prestack Kirchhoff migration. Different aspects of the numerical implementation are illustrated with numerical examples from a focusing gaussian-lens model. This model can be represented in terms of analytical gaussian functions as well as a computational grid. The model gives a fairly complicated and challenging ray pattern, including multipathing, caustics and wavefront triplications, such that several interesting aspects of ray tracing can be illustrated.

The numerical ray tracer is designed to be used in seismic imaging and inversion schemes. Therefore only transmitted rays in smooth media are considered. The particular present and future applications that we have in mind are implementation of 3-D anisotropic elastic multicomponent Kirchhoff migration (Hokstad, 1999,2000), computation of 3-D Maslov asymptotic Greens's functions in anisotropic media Brandsberg-Dahl et al. (2000), and 3-D anisotropic Maslov GRT (de Hoop and Brandsberg-Dahl, 1999)

2 Anisotropic elastic ray theory

This section gives a summary of the theory of anisotropic elastic ray tracing, following the work of Cerveny (1995). The ray theory will be presented in Cartesian coordinates because anisotropic ray tracing is implemented most efficiently in this coordinate system. In anisotropic media, the eigenvectors of the Christoffel equation, which will be discussed below, form a natural basis for the polarization of the rays. Consequently, the ray-centered coordinates and ray-centered basis vectors usually met in isotropic ray tracing become redundant in anisotropic media. In this section we use tensor notation, e.g. $\boldsymbol{x} = (x_1, x_2, x_3)$. Repeated Latin subscript indices are summed according to Einsteins summation convention.

2.1 Geometrical ray Green's tensor

The wave equation for the anisotropic elastic displacement Green's tensor γ_{in} in the frequency domain is given by

$$\omega^2 \rho(\boldsymbol{x}) \gamma_{in}(\boldsymbol{x}|\boldsymbol{x}_0) + \partial_j c_{ijkl}(\boldsymbol{x}) \partial_k \gamma_{ln}(\boldsymbol{x}|\boldsymbol{x}_0) = -\delta_{in} \delta(\boldsymbol{x} - \boldsymbol{x}_0), \tag{1}$$

where ρ is the density, c_{ijkl} is the Hooke's tensor, $\delta(\boldsymbol{x})$ is Dirac's delta function, and δ_{in} is Kronecker's delta function. In the geometrical ray approximation (GRA), the solution to equation (1) can be written as

$$\gamma_{ij}^{(mn)}(\boldsymbol{x}|\boldsymbol{x}_0) = \frac{\mathcal{A}(\boldsymbol{x}, \boldsymbol{x}_0) \mathrm{e}^{i(\pi/2)\mathrm{sgn}(\omega)\sigma}}{4\pi \mathcal{L}(\boldsymbol{x}, \boldsymbol{x}_0)} g_i^{(m)}(\boldsymbol{x}) g_j^{(n)}(\boldsymbol{x}_0) \mathrm{e}^{i\omega T(\boldsymbol{x}, \boldsymbol{x}_0)}, \tag{2}$$

where T is the traveltime along the ray, $\mathcal{L}$ is the relative geometrical spreading, which is reciprocal, σ is the KMAH index, and $g_j^{(n)}$ and $g_i^{(m)}$ are normalized polarization vectors on the source and receiver sides for wavemodes $(m, n) = 1, 2$ or 3, corresponding to $qS1$, $qS2$ or qP waves, respectively. The amplitude function is given by

$$\mathcal{A}(\boldsymbol{x}, \boldsymbol{x}_0) = \frac{\mathcal{R}^c(\boldsymbol{x}, \boldsymbol{x}_0)}{[Z(\boldsymbol{x})Z(\boldsymbol{x}_0)]^{1/2}}, \tag{3}$$

where $Z = \rho v_{ph}$, v_{ph} is the phase velocity and $\mathcal{R}^c$ is the product of reflection and transmission coefficients along the ray, normalized with respect to energy flux.

2.2 Christoffel equation

Substituting the GRA Green's tensor, equation (2), in the elastic wave equation, and assuming that the elastic medium varies slowly compared to the traveltime function, $T(\boldsymbol{x})$, we obtain the Christoffel equation

$$(\Gamma_{ik} - \delta_{ik})g_k^{(m)} = 0. \tag{4}$$

The Christoffel tensor is defined by

$$\Gamma_{ik} = \frac{c_{ijkl}}{\rho} p_j p_l, \tag{5}$$

where $p_j = \partial_j T(\boldsymbol{x})$ is the slowness. The Christoffel tensor is symmetric,

$$\Gamma_{ik} = \Gamma_{ki}, \tag{6}$$

and it is a homogeneous function of second degree in p_i, which implies that

$$\Gamma_{ik}(ap_j) = a^2 \Gamma_{ki}(p_j). \tag{7}$$

In an anisotropic elastic medium, the Christoffel equation (4) has three different eigenvalues given by

$$\det(\Gamma_{ik} - G^{(m)}\delta_{ik}) = 0. \tag{8}$$

The corresponding eigenvectors $g_k^{(m)}$ are obtained from

$$(\Gamma_{ik} - G^{(m)}\delta_{ik})g_k^{(m)} = 0, \tag{9}$$

with the normalization condition

$$g_k^{(m)} g_k^{(m)} = 1. \tag{10}$$

The eigenvectors represent the mutually orthogonal polarization directions of the quasi P and S modes, qP, qS1, qS2, which can propagate in an anisotropic elastic medium. Using equation (9), the eigenvalues can be rewritten as

$$G^{(m)} = \Gamma_{ik} g_i^{(m)} g_k^{(m)}. \tag{11}$$

In isotropic media, and for certain symmetry directions in anisotropic media, the eigenvalues are degenerate. Physically, this means that the phase velocities of the qS1 and qS2 waves are equal. According to the Christoffel equation (4), the existence condition for a ray is

$$G^{(m)}(p_i) = 1, \tag{12}$$

which is the eikonal equation for an anisotropic medium. The eigenvalues are homogeneous functions of second degree in p_j, like Γ_{ik}. Hence, the phase velocity satisfy the relation

$$v_{ph} = [G^{(m)}(n_i)]^{1/2}, \tag{13}$$

where $n_i = v_{ph} p_i$ is the normalized phase direction.

2.3 Kinetic ray tracing system

The eikonal equation (12) can be solved by the method of characteristics (Bleistein, 1984). To derive the system of linear differential equations for the ray, it is convenient to use the Hamiltonian formulation of classical mechanics (Goldstein, 1980). In the Hamiltonian formulation, ray position x_i and slowness p_i are considered as independent variables in the 6-D phase space. Hence, kinetic ray tracing corresponds to the computation of trajectories in the phase space. If the eikonal equation is expressed in the form of an Hamiltonian,

$$\mathcal{H}(x_i, p_i) = \frac{1}{2}(G^{(m)} - 1) = 0, \tag{14}$$

the equations of motion for the ray can be computed from Hamilton's canonical equations

$$\begin{aligned} \dot{x}_i &= \frac{\partial \mathcal{H}}{\partial p_i} = \frac{1}{2}\frac{\partial G^{(m)}}{\partial p_i}, && (15) \\ \dot{p}_i &= -\frac{\partial \mathcal{H}}{\partial x_i} = -\frac{1}{2}\frac{\partial G^{(m)}}{\partial x_i}. && (16) \end{aligned}$$

Here, $\dot{x}_i = \partial x_i / \partial T$ and $\dot{p}_i = \partial p_i / \partial T$ denote derivatives of ray position and slowness with respect to the traveltime T along the ray. Moreover, $\dot{x}_i$ can be identified as a component of the group velocity vector. Hence, the magnitude of the group velocity is given by

$$v_{gr} = [\dot{x}_i \dot{x}_i]^{1/2}. \tag{17}$$

Using equation (11), the kinetic ray tracing system in Cartesian coordinates can be written as

$$\begin{aligned} \dot{x}_i &= \frac{1}{2}\frac{\partial \Gamma_{jk}}{\partial p_i} g_j^{(m)} g_k^{(m)}, && (18) \\ \dot{p}_i &= -\frac{1}{2}\frac{\partial \Gamma_{jk}}{\partial x_i} g_j^{(m)} g_k^{(m)}, && (19) \end{aligned}$$

The initial conditions for the kinetic ray tracing system are

$$\begin{aligned} x_i(T_0) &= x_{i0}, && (20) \\ p_i(T_0) &= p_{i0} = \frac{n_{i0}}{v_{ph}(\boldsymbol{x}_0)}. && (21) \\ & && (22) \end{aligned}$$

where p_{i0} and $v_{ph}(\boldsymbol{x}_0)$ fulfill the eikonal equations (11) and (13). The initial phase direction $\boldsymbol{n}_0 = (n_{10}, n_{20}, n_{30})$ can be expressed in terms of the initial polar and azimuth phase angles θ_0 and ϕ_0, see Figure 1,

$$\begin{aligned} n_{10} &= \sin\theta_0 \cos\phi_0, \\ n_{20} &= \sin\theta_0 \sin\phi_0, \\ n_{30} &= \cos\theta_0. \end{aligned} \tag{23}$$

2.4 Dynamic ray tracing system

The most important application of dynamic ray tracing is computation of the relative geometrical spreading $\mathcal{L}$ appearing in the amplitude function of the GRA Green's tensor. The dynamic ray tracing system in Cartesian coordinates is given by

$$\begin{aligned} \dot{Q}_{iK} &= \frac{\partial^2 \mathcal{H}}{\partial p_i \partial x_j} Q_{jK} + \frac{\partial^2 \mathcal{H}}{\partial p_i \partial p_j} P_{jK}, && (24) \\ \dot{P}_{iK} &= -\frac{\partial^2 \mathcal{H}}{\partial x_i \partial x_j} Q_{jK} - \frac{\partial^2 \mathcal{H}}{\partial x_i \partial p_j} P_{jK}, && (25) \end{aligned}$$

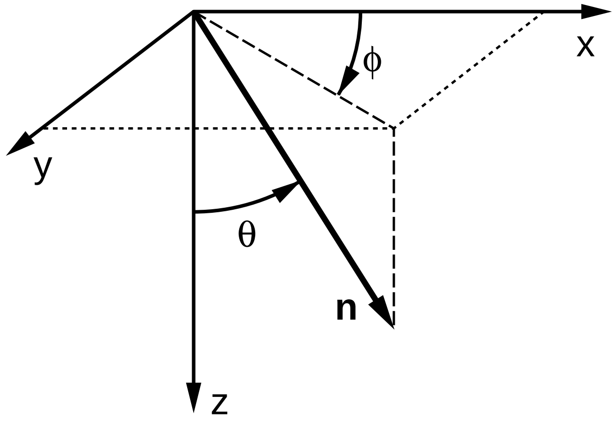

Figure 1: The normalized phase direction $\boldsymbol{n} = (n_1, n_2, n_3)$ can be represented by polar θ and azimuth ϕ phase angles.

where the $i, j = 1, 2, 3$ and $K = 1, 2$. The 3 × 2 matrices Q_{iK} and P_{iK} are defined by

$$Q_{iK} = \frac{\partial x_i}{\partial \gamma_K}, \tag{26}$$

$$P_{iK} = \frac{\partial p_i}{\partial \gamma_K}, \tag{27}$$

where (γ_1, γ_2) are two ray parameters that define the local phase direction of the ray, e.g. $(\gamma_1, \gamma_2) = (\theta, \phi)$. The second derivatives of the Hamiltonian $\mathcal{H}$ are given by the equations

$$\frac{\partial^2 \mathcal{H}}{\partial p_i \partial p_j} = \frac{1}{2}\frac{\partial^2 \Gamma_{kl}}{\partial p_i \partial p_j} g_k^{(m)} g_l^{(m)} + \frac{\partial \Gamma_{kl}}{\partial p_i} g_k^{(m)} \frac{\partial g_l^{(m)}}{\partial p_j}, \tag{28}$$

$$\frac{\partial^2 \mathcal{H}}{\partial p_i \partial x_j} = \frac{1}{2}\frac{\partial^2 \Gamma_{kl}}{\partial p_i \partial x_j} g_k^{(m)} g_l^{(m)} + \frac{\partial \Gamma_{kl}}{\partial x_i} g_k^{(m)} \frac{\partial g_l^{(m)}}{\partial p_j}, \tag{29}$$

$$\frac{\partial^2 \mathcal{H}}{\partial x_i \partial p_j} = \frac{1}{2}\frac{\partial^2 \Gamma_{kl}}{\partial x_i \partial p_j} g_k^{(m)} g_l^{(m)} + \frac{\partial \Gamma_{kl}}{\partial x_i} g_k^{(m)} \frac{\partial g_l^{(m)}}{\partial p_j}, \tag{30}$$

$$\frac{\partial^2 \mathcal{H}}{\partial x_i \partial x_j} = \frac{1}{2}\frac{\partial^2 \Gamma_{kl}}{\partial x_i \partial x_j} g_k^{(m)} g_l^{(m)} + \frac{\partial \Gamma_{kl}}{\partial x_i} g_k^{(m)} \frac{\partial g_l^{(m)}}{\partial x_j}. \tag{31}$$

From the normalization condition $g_i^{(m)} g_i^{(m)} = 1$ it follows that

$$\frac{\partial g_k^{(m)}}{\partial y} g_k^{(m)} = 0, \tag{32}$$

where $y = x_j$ or $y = p_j$. Hence, if the eigenvalues of the Christoffel equation (5) are nondegenerate, $\partial g_k^{(m)}/\partial y$ and $g_k^{(m)}$ are orthogonal. Then $\partial g_k^{(m)}/\partial y$ can be written as a linear combination of the other two eigen vectors,

$$\frac{\partial g_k^{(m)}}{\partial y} = A^{(p)} g_k^{(p)} + A^{(q)} g_k^{(q)}, \ \ (p) \neq (q) \neq (m). \tag{33}$$

By means of the Christoffel equation (5), the Coefficients $A^{(p)}$ can be expressed as

$$A^{(p)} = \frac{1}{G^{(p)} - G^{(m)}} \frac{\partial \Gamma_{kl}}{\partial y} g_k^{(m)} g_k^{(p)}, \ \ (p) \neq (m), \tag{34}$$

where $G^{(m)} = 1$ (from the eikonal equation) and $G^{(p)} = (v_{ph}^{(p)}/v_{ph}^{(m)})^2$. For computation of geometrical spreading, we are interested in the solution of the dynamic ray tracing system with point source initial conditions. The point source initial conditions in a Cartesian coordinate system can be written as

$$Q_{iK0} = 0, \tag{35}$$

$$Q_{iK0} = H_{iK0} - p_{i0}\dot{x}_{j0}H_{jK0}, \tag{36}$$

where p_{i0} are given by equations (21) and (23), and H_{iK} is the transformation from ray-centered to Cartesian coordinates,

$$H_{ij} = \frac{\partial x_i}{\partial y_j}, \tag{37}$$

where x_j are (global) Cartesian coordinates and y_j are (local) ray-centered Cartesian coordinates.

2.5 Geometrical spreading

The relative geometrical spreading is commonly expressed as

$$\mathcal{L}(\boldsymbol{x}, \boldsymbol{x}_0) = [\det \boldsymbol{Q}_2]^{1/2}, \tag{38}$$

where $\boldsymbol{Q}_2$ is a 2×2 matrix in ray-centered coordinates. In Cartesian coordinates, the relative geometrical spreading, can be written as

$$\mathcal{L}(\boldsymbol{x}, \boldsymbol{x}_0) = \left[\frac{\det \boldsymbol{Q}}{v_{ph}}\right]^{1/2} \tag{39}$$

where Q_{iK} is a solution of the dynamic ray tracing system with point source initial conditions. The third column of the matrix $\boldsymbol{Q}$ is given by

$$Q_{i3} = \dot{x}_i. \tag{40}$$

3 Numerical ray tracing

We present in some detail the numerical implementation of a 3-D anisotropic elastic initial-value ray tracer. Moreover, we discuss the interpolation of ray-tracing data and of the geological model which is required when input and output data are given on regular grids. In this section, we will use the notation $\boldsymbol{x} = (x, y, z)$ etc. to refer to 3-D Cartesian coordinates. Subscripts will mostly be used to label discrete points, e.g. the coordinates of the vector $\boldsymbol{x}_k$ are (x_k, y_k, z_k).

3.1 Numerical test model

Different aspects of the numerical implementation will be illustrated with a simple but interesting numerical example as we go along. The 3-D geological model is a focusing Gaussian lens with TIV symmetry. The model can be represented analytically by the equation

$$C_{IJ}(x,y,z) = C_{IJ}^0\left[1 + K\exp\left\{-\left(\frac{(x-x_c)^2}{\sigma_x^2} + \frac{(y-y_c)^2}{\sigma_y^2} + \frac{(z-z_c)^2}{\sigma_z^2}\right)\right\}\right]. \tag{41}$$

The numerical values used are

$$\begin{aligned} K &= -0.6, \\ \sigma_x = \sigma_y = \sigma_z &= 50 \text{ m}, \\ x_c = y_c = z_c &= 500 \text{ m}, \end{aligned}$$

where (x_c, y_c, z_c) is the center of the Gaussian lens. We will also use a 2-D model (Gaussian "hot-dog") obtained by setting $\sigma_y = \infty$ and a 1-D model (Gaussian "pizza") obtained by setting $\sigma_x = \sigma_y = \infty$. The elastic moduli C^0_{IJ} in the 6×6 Voigt matrix representation are given by

$$\begin{aligned}
C^0_{11} &= 2.016 \text{ GPa} , \quad C^0_{33} = 1.440 \text{ GPa} , \\
C^0_{13} &= 0.855 \text{ GPa} , \quad C^0_{12} = 0.224 \text{ GPa} , \\
C^0_{44} &= 0.360 \text{ GPa} , \quad C^0_{66} = 0.396 \text{ GPa} ,
\end{aligned}$$

This Voigt matrix corresponds to

$$V_{P0} = 1200 \text{ m/s} , \quad V_{S0} = 600 \text{ m/s} , \quad \epsilon = 0.20, \quad \delta = 0.10, \quad \gamma = 0.05, \tag{42}$$

where V_{P0} and V_{S0} are the vertical P- and S-wave velocities and ϵ, δ and γ are the Thomsen parameters. The density $\rho = 1000.0$ kg/m^3 is constant. The same model was used in the work of Kendall et al. (1992). In the numerical ray-tracing examples, we will use initial polar angles θ and phase angles ϕ in the intervals

$$0 \leq \theta \leq \frac{\pi}{6} = 30^\circ, \quad 0 \leq \phi \leq 2\pi = 360^\circ. \tag{43}$$

3.2 Initial value ray tracing

We perform initial-value ray tracing by numerical integration of the kinetic and dynamic ray tracing systems using a fifth-order embedded Runge-Kutta method. The ray tracing is performed in a 3-D anisotropic elastic velocity model for a user-defined set of initial polar and azimuth phase angles. The kinetic and dynamic ray tracing systems are linear systems of coupled first-order differential equations which can be written in the generic form

$$\dot{\boldsymbol{y}} = \boldsymbol{f}(\boldsymbol{y}), \tag{44}$$

where $\boldsymbol{y}$ and $\boldsymbol{f}$ are N-component vectors. For the kinetic ray tracing system, $N = 6$ and $\boldsymbol{y}$ is given by

$$\boldsymbol{y} = (x_i, p_i)^T, \quad i = 1, 2, 3, \tag{45}$$

The vector $\boldsymbol{f}$ is correspondingly given by the right-hand side of equations (18) and (19). For the dynamic ray tracing system $N = 12$ and $\boldsymbol{y}$ is given by

$$\boldsymbol{y} = (Q_{iK}, P_{iK})^T, \quad i = 1, 2, 3, \; K = 1, 2, \tag{46}$$

The vector $\boldsymbol{f}$ is correspondingly given by equations (24) and (25.) In equations (45) and (46), we have used the tensor notation of the previous section. The general fifth-order Runge-Kutta formula for the generic equation (44) can be written as (Press et al., 1992)

$$\begin{aligned}
\boldsymbol{k}_1 &= \Delta t \boldsymbol{f}(\boldsymbol{y}_n), && (47)\\
\boldsymbol{k}_2 &= \Delta t \boldsymbol{f}(\boldsymbol{y}_n + b_{21}\boldsymbol{k}_1), && (48)\\
&\cdots \\
\boldsymbol{k}_6 &= \Delta t \boldsymbol{f}(\boldsymbol{y}_n + b_{61}\boldsymbol{k}_1 + b_{62}\boldsymbol{k}_2 + \cdots b_{65}\boldsymbol{k}_6), && (49)\\
\boldsymbol{y}_{n+1} &= \boldsymbol{y}_n + c_1\boldsymbol{k}_1 + c_2\boldsymbol{k}_2 + \cdots c_6\boldsymbol{k}_6 + \mathcal{O}(\Delta t^6), && (50)
\end{aligned}$$

where $\boldsymbol{y}_n$ is the Runge-Kutta solution at the n-th integration step, and $\boldsymbol{k}_i$, $i = 1, 2, \cdots, 6$, are temporary N-component vectors. The embedded fourth-order formula is

$$\hat{\boldsymbol{y}}_{n+1} = \boldsymbol{y}_n + \hat{c}_1\boldsymbol{k}_1 + \hat{c}_2\boldsymbol{k}_2 + \cdots + \hat{c}_6\boldsymbol{k}_6 + \mathcal{O}(\Delta t^5). \tag{51}$$

The numerical coefficients a_i, b_{ij}, c_i and $\hat{c}_i$ are given in Table 1. Using six evaluations of the right-hand

i	a_i	b_{i1}	b_{i2}	b_{i3}	b_{i4}	b_{i5}	c_i	$\hat{c}_i$
1							$\frac{37}{378}$	$\frac{2835}{27648}$
2	$\frac{1}{5}$	$\frac{1}{5}$					0	0
3	$\frac{3}{10}$	$\frac{3}{40}$	$\frac{9}{40}$				$\frac{250}{621}$	$\frac{18575}{48384}$
4	$\frac{3}{5}$	$\frac{3}{10}$	$\frac{-9}{10}$	$\frac{6}{5}$			$\frac{125}{594}$	$\frac{13525}{55296}$
5	1	$\frac{-11}{54}$	$\frac{5}{2}$	$\frac{-70}{27}$	$\frac{35}{27}$		0	$\frac{277}{14336}$
6	$\frac{7}{8}$	$\frac{1631}{55296}$	$\frac{175}{512}$	$\frac{575}{13824}$	$\frac{44275}{110592}$	$\frac{253}{4096}$	$\frac{512}{1771}$	$\frac{1}{4}$

Table 1: Numerical coefficients for fifth order embedded Runge-Kutta integration.

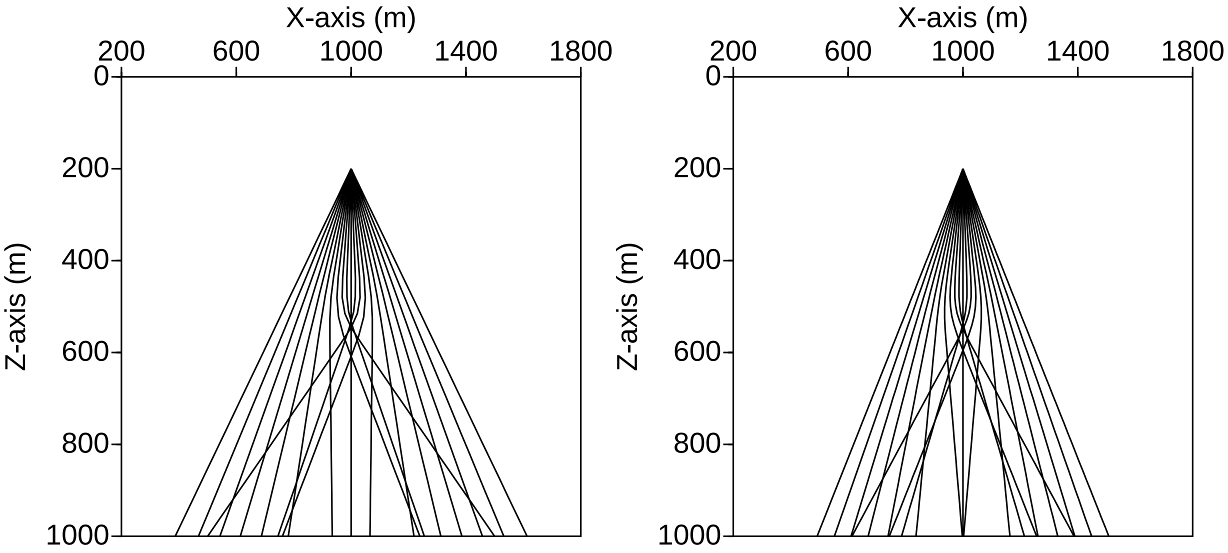

Figure 2: Ray paths in the vertical plane $y = 1000$ m of the 3-D Gaussian lens model. The source is located at $\boldsymbol{x} = (1000, 1000, 200)$ m. qP-rays (left) and $qS1$-rays (right).

side it also provides an estimate of the truncation error $\boldsymbol{\Delta}$ which can be written as

$$\boldsymbol{\Delta} = \boldsymbol{y}_{n+1} - \hat{\boldsymbol{y}}_{n+1} = \sum_{i=1}^{6} (c_i - \hat{c}_i)\boldsymbol{k}_i. \tag{52}$$

The error estmate can be used for adaptive stepsize control. If Δt_1 is the current stepsize with corresponding error estimete $\boldsymbol{\Delta}_1$, and if $\boldsymbol{\Delta}_0$ is the desired accuracy, the new stepsize Δt_0 can be written as

$$\Delta t_0 = \left\{ \begin{array}{ll} S \Delta t_1 \left| \boldsymbol{\Delta}_0 / \boldsymbol{\Delta}_1 \right|^{0.20}, & |\boldsymbol{\Delta}_0| \geq |\boldsymbol{\Delta}_1| \\ S \Delta t_1 \left| \boldsymbol{\Delta}_0 / \boldsymbol{\Delta}_1 \right|^{0.25}, & |\boldsymbol{\Delta}_0| < |\boldsymbol{\Delta}_1| \end{array} \right. , \tag{53}$$

where $S \leq 1$ is a safety factor, typically $S \simeq 0.9$. The numerical implementation is adapted from the subroutines `rkck` and `rkqs` given in *Numerical Recipes in Fortran* (Press et al., 1992).

Figure 2 shows a numerical examples of qP and $qS1$ rays in the the vertical plane $y = 1000$ m. The source is in the same plane. The ray trajectories were computed by Runge-Kutta integration of the kinetic ray tracing system in the 3-D Gaussian-lens model.

3.3 Uniform distribution of rays

The 3-D initial-value ray tracing is performed for a discrete set of initial polar angles θ and azimuth angles ϕ such that

$$0 \leq \quad \theta \quad \leq \theta_{max}, \tag{54}$$

$$0 \leq \quad \phi \quad < 2\pi, \tag{55}$$

where the maximum polar angle $\theta_{max} \leq \pi/2$ is chosen by the user. In relatively simple elastic media, e.g. a 1-D medium, we expect that the offset of the ray increases with increasing initial polar angle. Hence, when the initial polar and azimuth angles are discretized, we would like to have a small increment in the azimuth angle when the polar angle is large, in order to obtain a dense coverage of rays in the elastic model. On the other hand, for small polar angles, a sufficient ray density can be achieved with a larger step in azimuth angle. In particular, the ray with zero polar angle needs to be computed only once.

The discretized polar angle can be written as

$$\theta_j = (j-1)\Delta\theta, \;\; j = 1, 2, \cdots, M, \tag{56}$$

where M is the number of a polar angles. To obtain a relatively uniform ray density, the azimuth angle should be discretized according to

$$(j-1)\Delta\theta\Delta\phi_j = const \tag{57}$$

The increment in azimuth angle depending on the polar angles θ_j, can be written as

$$\Delta\phi_j = \frac{2\pi}{N_j} \tag{58}$$

where N_j is the number of azimuth directions, Substituting equation (58) in equation (57), we get

$$N_j = \frac{j-1}{j-2} N_{j-1} = (j-1)N_2, \;\; j = 3, 4, 5 \cdots, \tag{59}$$

where N_2 is a small number which must be specified by the user, and $N_1 = 1$. Equation (59) does a fairly good job in relatively simple elastic media. If a uniform distribution of rays in general media is desired, the ray tracing must be performed with the wavefront-construction method (Vinje et al., 1993).

Figure 3 shows a numerical example from 3-D initial-value ray tracing in the 1-D Gaussian model, where $N_2 = 6$.

3.4 Interpolation of rays at constant depth

The Runge-Kutta algorithm described above, equations (47) to (50), performs kinetic and dynamic initial-value ray tracing, stepping ray position x_i, slowness p_i and ray propagators Q_{iK} and P_{iK} forward in time. Here, time means traveltime $T(\boldsymbol{x})$ along the ray. Consequently, to obtain ray-tracing data at prescribed spatial receiver positions, e.g. a regular grid, interpolation is required. We perform interpolation of ray tracing data on a regular 3-D grid by means of a two-step procedure.

1. Interpolation to selected planes of constant depth.
2. Interpolation in each constant-depth plane to obtain ray tracing data on the 3-D grid.

In this section, we discuss the first interpolation step. The second step is discussed in the next section.

The interpolation to depth levels $z = constant$ is performed by a cubic spline along each ray. Let $h(\boldsymbol{x})$ represent traveltime T, ray position x_i, slowness p_i, polarization $g_i^{(m)}$ or geometrical spreading $\mathcal{L}$

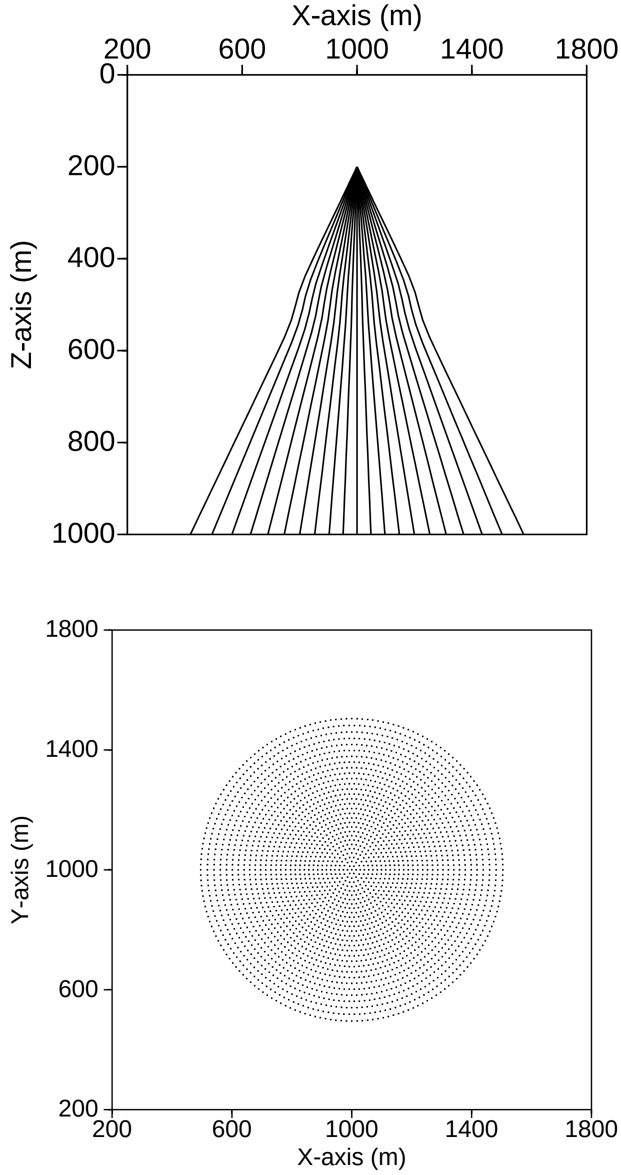

Figure 3: 3-D initial-value ray tracing in the 1-D Gaussian model. qP-rays in a vertical plane (top) and ray-intersections with the horizontal plane at depth $z = 900.0m$ (bottom).

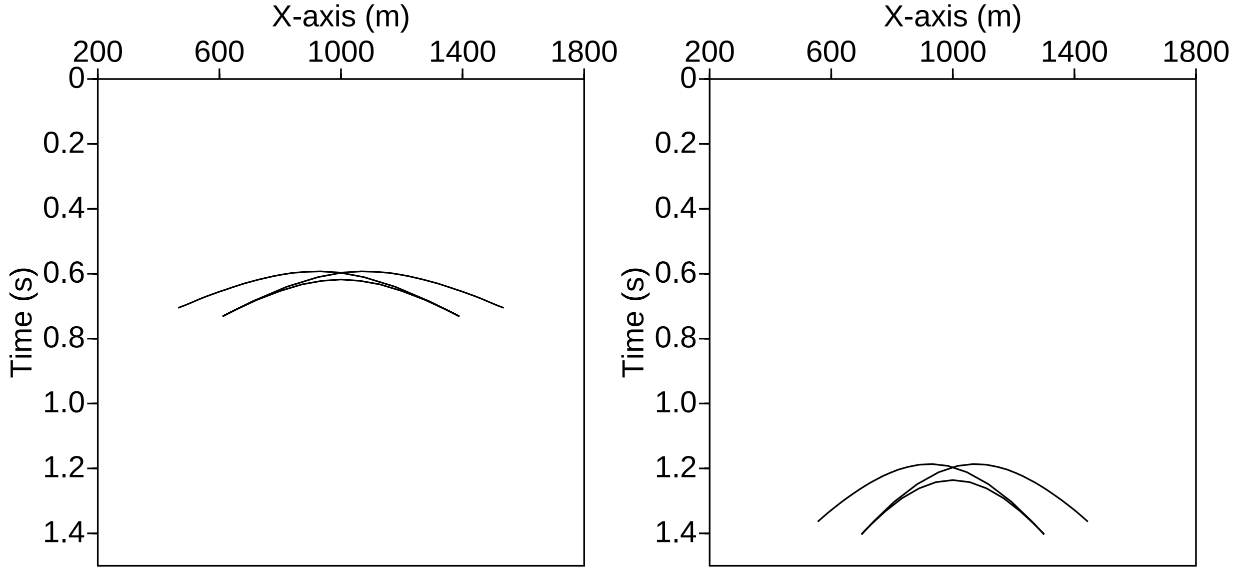

Figure 4: Traveltimes at depth $z = 900$ m. 3-D Gaussian model. qP-rays (left) and $qS1$-rays (right).

along the ray. Then, the cubic spline approximation to $h(\boldsymbol{x})$ is a piecewise cubic polynomial which can be written as

$$h(\boldsymbol{x}) \simeq S(\xi) = \begin{cases} S_1(\xi), & \xi_1 \leq \xi \leq \xi_2, \\ S_2(\xi), & \xi_2 \leq \xi \leq \xi_3, \\ \cdots & \\ S_{N_S-1}(\xi), & \xi_{N_S-1} \leq \xi \leq \xi_{N_S}, \end{cases} \tag{60}$$

where $S_j(\xi)$ is a cubic polynomial

$$S_j(\xi) = A_j\xi^3 + B_j\xi^2 + C_j\xi + D_j, \;\; \xi_j \leq \xi \leq \xi_{j+1}, \tag{61}$$

and $\xi = \xi(z)$ is a monotonic parameter along the ray. The coefficients A_j, B_j, C_j, D_j are chosen such that $S(\xi)$ is smooth and $\partial_\xi S$ and $\partial^2_\xi S$ are contineous at $\xi = \xi_j, \; j = 1, 2, \cdots, N_S$ (called the knots). From the ray tracing, the N_S values of $S(\xi_j)$ (called nodes) are known. The node values and the continuity conditions provide $2(N_S - 1) + 2(N_S - 1)$ conditions for $4(N_S - 1)$ unknowns. To obtain the last 2 conditions, we can specify the second-derivatives at the endpoints. Chosing

$$\partial^2_\xi S(\xi_1) = \partial^2_\xi S(\xi_{N_S}) = 0, \tag{62}$$

the spline is a natural cubic spline. Cubic splines lead to tridiagonal systems of linear equations, which can be solved efficiently in $\mathcal{O}(N)$ numerical operations.

The parameter ξ must be monotonically increasing along the ray such that $S(\xi)$ is a single-valued function. If turning waves are excluded, we may choose $\xi = z$ which gives the numerically most efficient implementation. To include turning rays, we can use $\xi = T$, but this requires the use of a search algorithm to determine $T = T(z)$ for given output depth z. Currently, we use the faster option $\xi = z$. The cubic-spline interpolation was implemented by means of the subroutines `spline` and `splint` from *Numerical Recipes in Fortran* (Press et al., 1992).

Figures 4 to 6 shows numerical examples from ray tracing in the 3-D Gaussian-lens model. Traveltimes, slowness and geometrical spreading for qP and $qS1$ rays are interpolated to depth $z = 900$ m using cubic splines.

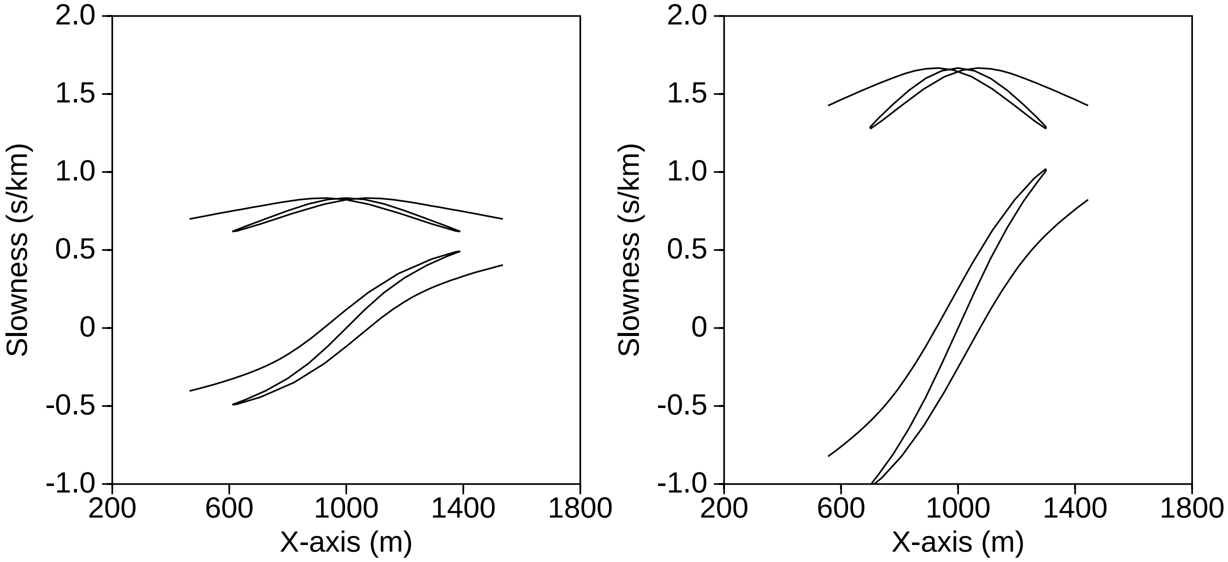

Figure 5: Slowness at depth $z = 900$ m. 3-D Gaussian model. qP-rays (left) and $qS1$-rays (right).

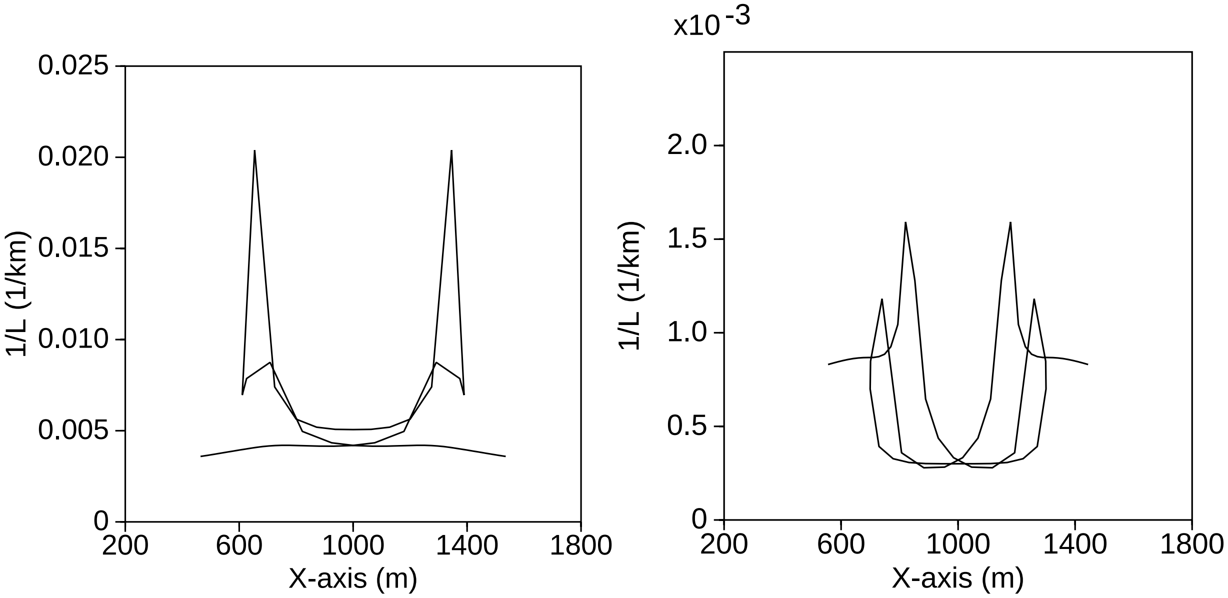

Figure 6: Relative geometrical spreading at depth $z = 900$ m. 3-D Gaussian model. qP-rays (left) and $qS1$-rays (right).

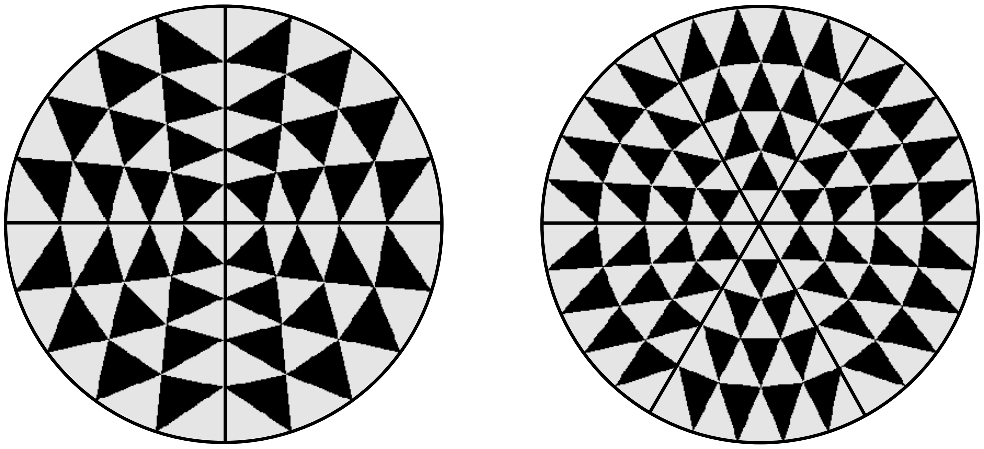

Figure 7: Triangulation of rays in the xy-plane for two different azimuthal ray densities, $N_1 = 4$ (left) and $N_1 = 6$ (right). The number of polar phase directions is 6

3.5 Interpolation of rays on a regular grid

The interpolation of ray tracing data to a regular 3-D grid is performed by linear interpolation in the xy-plane for each depth level z of interest. The input data are the results from the spline interpolation along each ray, as described in the previous section.

The interpolation is performed by a triangulation of neighboring ray-intersections at each depth level. Then the linear interpolation is performed by fitting a plane through the vertices of the triangle. The main challenge is to insure that there are no void grid cells in the interpolated data and to account for multipathing. In a smooth elastic model, all ray-theoretical quantities are continuous single-valued functions of the initial polar and azimuth angles. To insure that there are no void grid cells left after the interpolation, we perform a sequential loop over initial phase angles. When we use equation (59) to determine the number of azimuth directions, the triangulation pattern becomes completely regular and predictable, such that no random search for neighboring rays is required. Figure 7 shows examples of the triangulation, in the xy-plane for a homogeneous model, for two different azimuthal ray densities. In complex media with multipathing, the triangulation becomes more complicated, but remains regular and predictable as a function of initial phase angles.

The purpose of the triangulation described above is to identify the three nearest neighboring rays which contribute to the interpolation of ray tracing data at each node of the 3-D regular grid. Again, let $h(\boldsymbol{x}) = h(x, y, z = z_0)$, where z_0 is constant, represent traveltime T, ray position x_i, slowness p_i, polarization $g_i^{(m)}$ or geometrical spreading $\mathcal{L}$ along the ray. The values $h(x_1, y_1, z_0)$, $h(x_2, y_2, z_0)$ and $h(x_3, y_3, z_0)$ at the vertices of the triangle define a linear plane which can be expressed in the form of a weighted average

$$h(x, y, z_0) \simeq \Sigma(x, y) = \sum_{k=1}^{3} w_k(x, y) h(x_k, y_k, z_0), \tag{63}$$

where

$$w_k(x, y) = \frac{W_k}{W_1 + W_2 + W_3}, \tag{64}$$

and

$$W_1(x, y) \quad = \quad (x - x_3)(y - y_2) - (x - x_2)(y - y_3), \tag{65}$$

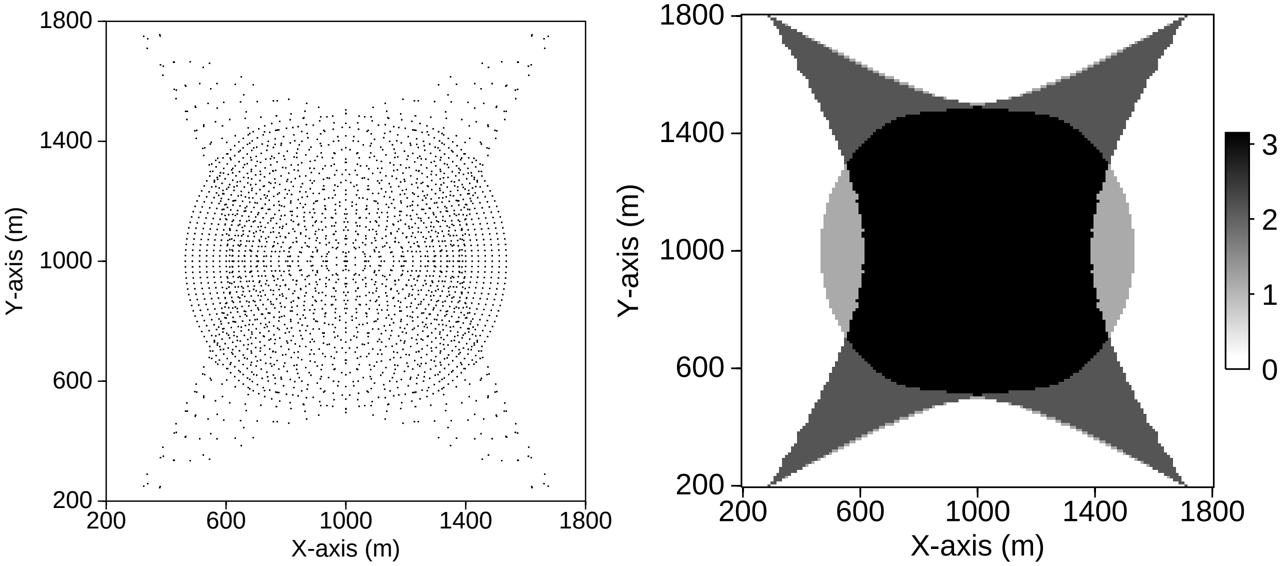

Figure 8: qP-rays intersecting the horizontal plane $z = 900$ m (left) and number of arrivals in each grid node (right). 2-D Gaussian-lens model.

$$W_2(x,y) = (x-x_1)(y-y_3)-(x-x_3)(y-y_1), \tag{66}$$

$$W_3(x,y) = (x-x_2)(y-y_1)-(x-x_1)(y-y_2). \tag{67}$$

If the interpolation point (x, y) is located on one of the lines connecting the vertices of the riangle, equation (63) reduces to 1-D linear interpolation. Equation (63) can be derived from the canonical equation of a plane (i.e. the formula ax+by+cz+d=0).

Figures 8 to 11 show a numerical example from the 2-D Gaussian-lens models. Figure 8 shows the intersection of the rays in the plane $z = 900$ m, and the number of arrivals in each grid point at this depth level for the 2-D model. Figures 9 to 11 show cross-sections of the traveltime, slowness and geometrical spreading interpolated on a regular grid. The cross-sections are from the vertical planes $y = y_s$ and $x = x_s - 50$ m, where (x_s, y_s) are the source coordinates. A corresponding example computed in the 3-D Gaussian-lens model is shown in Figures 12 to 15.

3.6 Interpolation of the geological model

The geological model is represented on a regular grid. In the Runge-Kutta integration of the kinetic and dynamic ray tracing system, the elastic coefficients of the geological model must be interpolated at ray positions $\boldsymbol{x}$ which are in general not on a grid node. We perform the interpolation of the elastic coefficients by means of polynomial interpolation on Lagrange form (Kincaid and Cheney, 1991).

Wang and Bleistein (1998) performed dynamic wavefront construction on a regular grid, but considered only isotropy and P-waves. They used linear interpolation of the bulk modulus and its derivatives. The first and second derivatives of the bulk modulus were precomputed by finite differencing. This approach is, however, not practical in anisotropic elastic media. For the simplest case of a TIV-medium, we need five 3-D grids for the elastic moduli. With precomputed first and second derivatives, this increases by a factor of ten. Wang and Bleistein concluded that 3-4 grid points per shortest wavelength of the model (measured in terms of the Fourier wavenumber), were needed to obtain the required accuracy.

We will first consider 1-D polynomial interpolation. Generalization to 3-D is straight-forward, as will be shown below. Let $g(x_i)$ denote discrete values of a function $g(x)$ at positions $x_i = (i-1)\Delta x,\ i =$

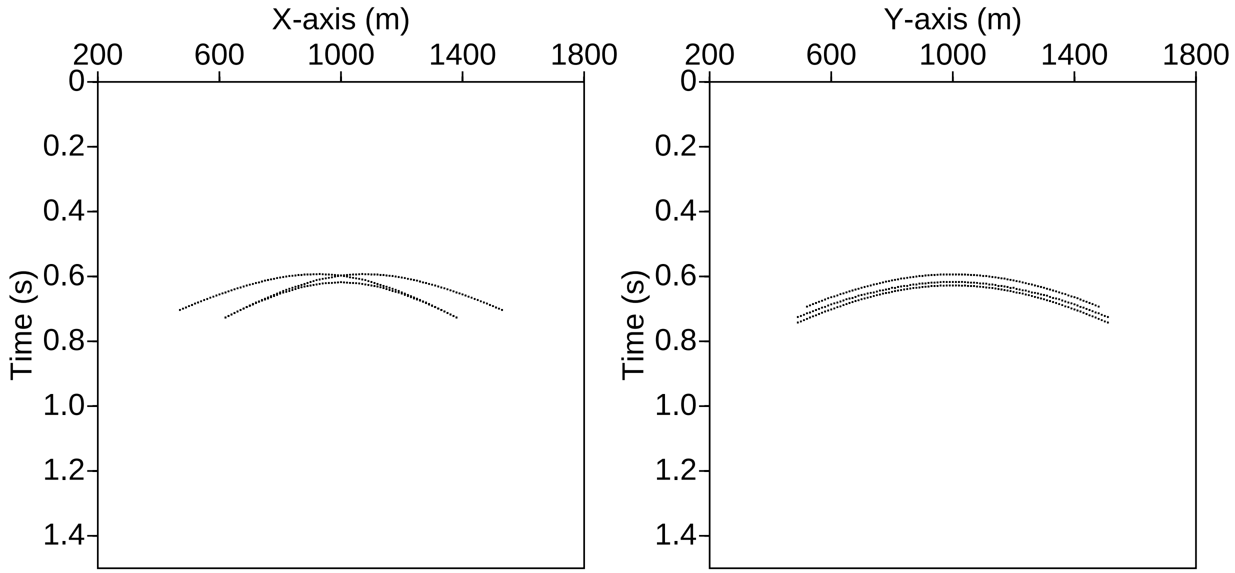

Figure 9: Traveltimes at depth $z = 900$ m, interpolated to a regular grid. 2-D Gaussian model. qP-rays. Cross-sections in the vertical planes $y = y_s = 1000$ m and $x = x_s - 50$ m $= 950$ m.

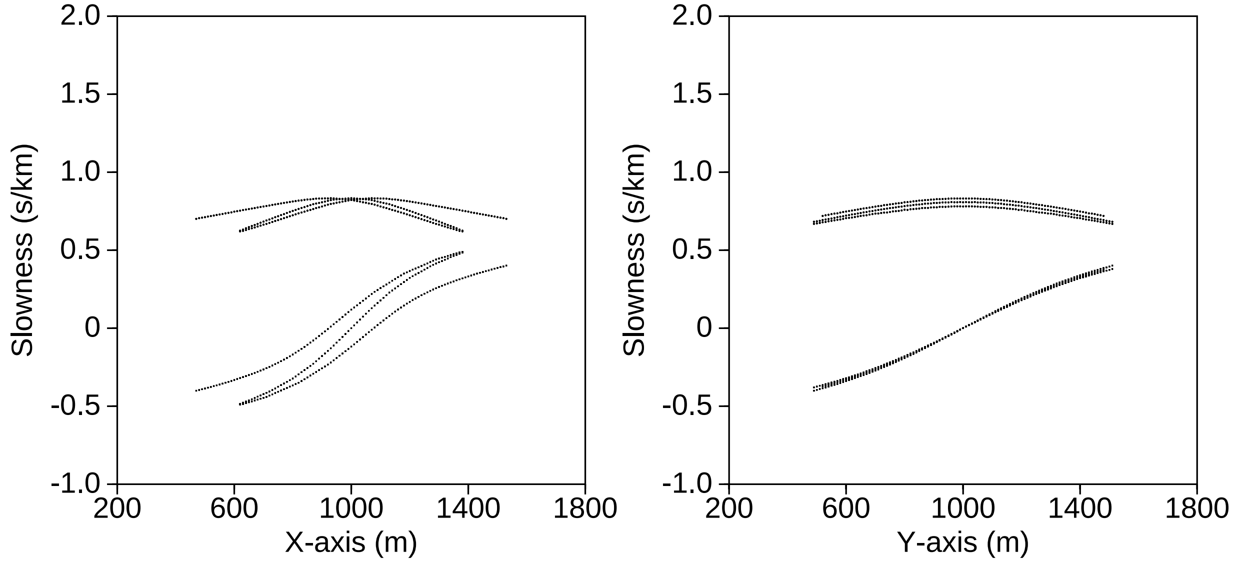

Figure 10: Slowness at depth $z = 900$ m, interpolated to a regular grid. 2-D Gaussian model. qP-rays. Cross-sections in the vertical planes $y = y_s = 1000$ m and $x = x_s - 50$ m $= 950$ m.

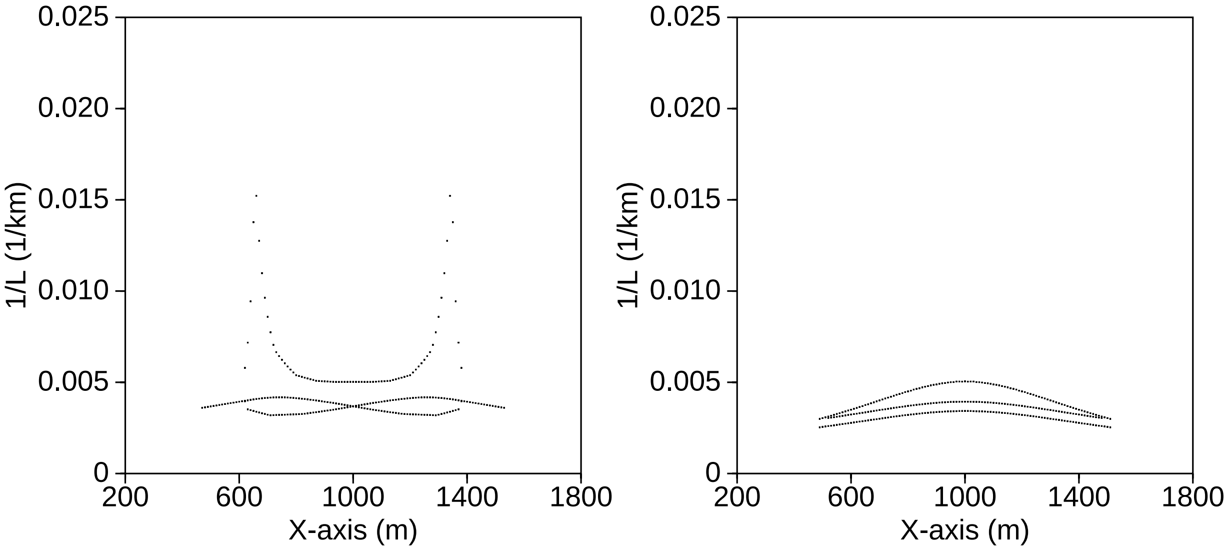

Figure 11: Relative geometrical spreading at depth $z = 900$ m, interpolated to a regular grid. 2-D Gaussian model. qP-rays. Cross-sections in the vertical planes $y = y_s = 1000$ m and $x = x_s - 50$ m $= 950$ m.

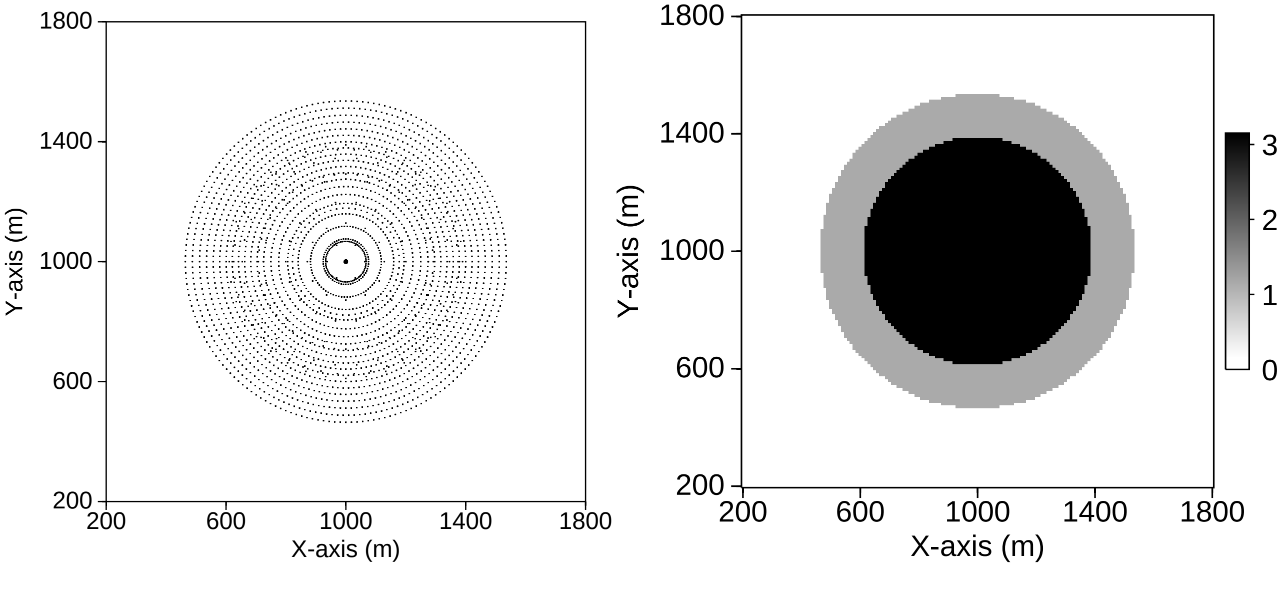

Figure 12: qP-rays intersecting the horizontal plane $z = 900$ m (left) and number of arrivals in each grid node (right). 3-D Gaussian-lens model.

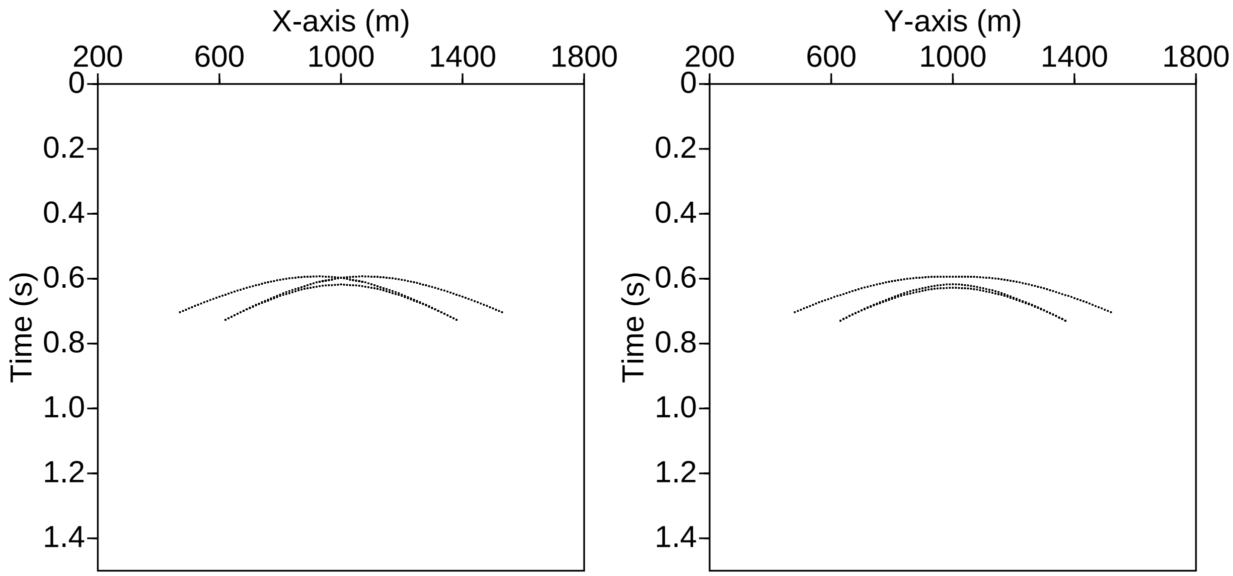

Figure 13: Traveltimes at depth $z = 900$ m, interpolated to a regular grid. 3-D Gaussian model. qP-rays. Cross-sections in the vertical planes $y = y_s = 1000$ m and $x = x_s - 50$ m $= 950$ m.

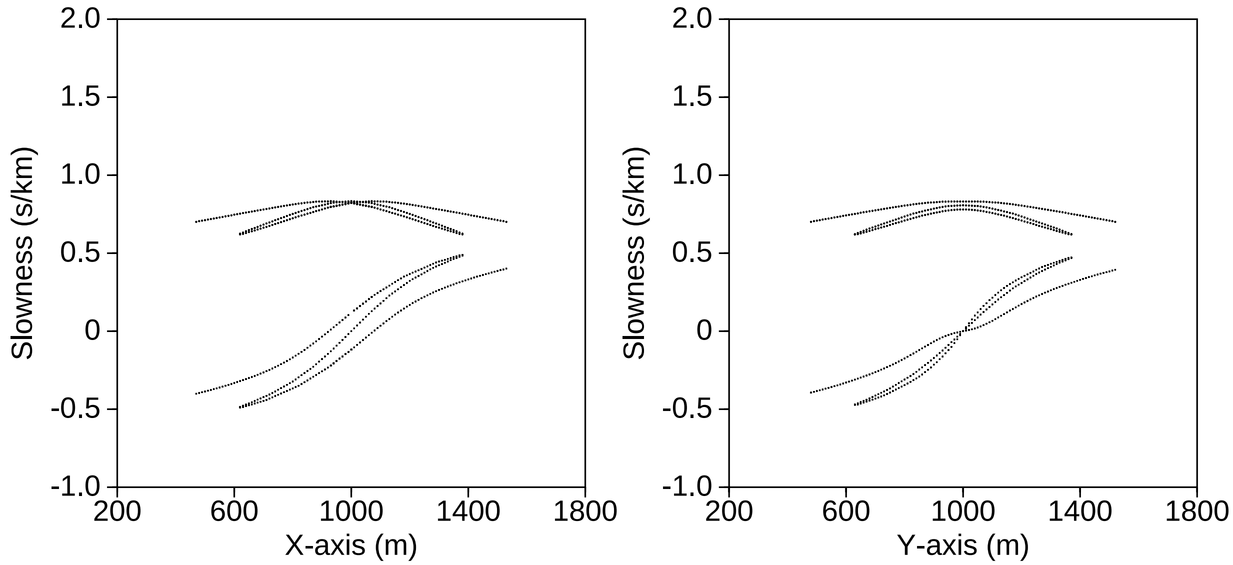

Figure 14: Slowness at depth $z = 900$ m, interpolated to a regular grid. 3-D Gaussian model. qP-rays. Cross-sections in the vertical planes $y = y_s = 1000$ m and $x = x_s - 50$ m $= 950$ m.

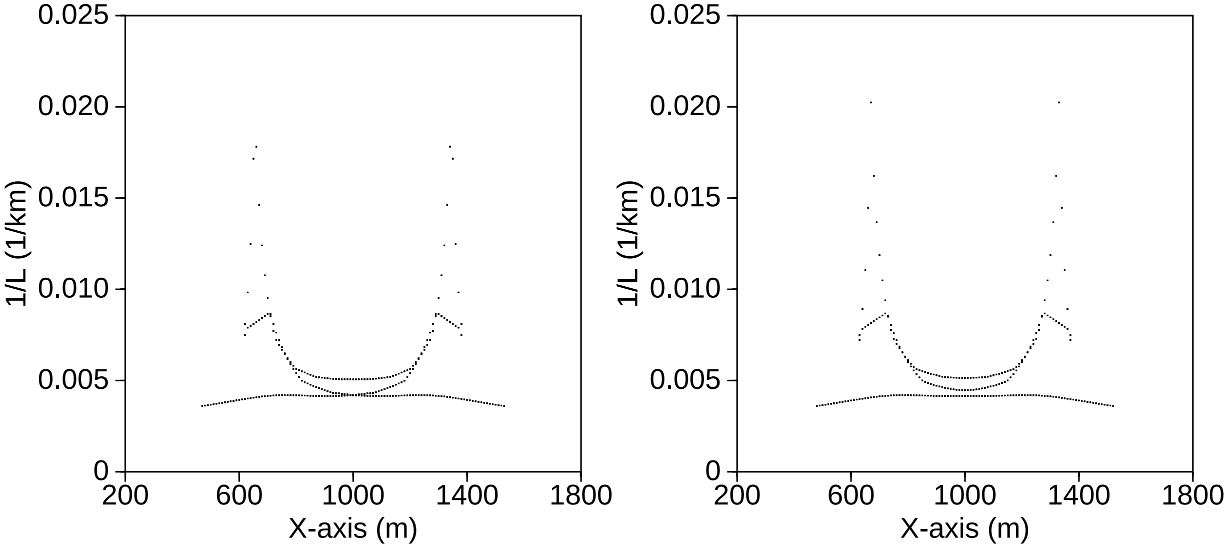

Figure 15: Relative geometrical spreading at depth $z = 900$ m, interpolated to a regular grid. 3-D Gaussian model. qP-rays. Cross-sections in the vertical planes $y = y_s = 1000$ m and $x = x_s - 50$ m $= 950$ m.

$1, 2, \cdots, I_P + 1$. The interpolated approximation to $g(x)$ can be written as

$$g(x) \simeq P(x) = \sum_{i=1}^{I_P+1} g(x_i)u_i(x) \tag{68}$$

where $P(x)$ is the interpolating polynomial of order I_P on Lagrange form. The interpolating polynomial is constructed from the I_P nearest neighbors of x. High-order interpolating polynomials are oscillating functions. Consequently, the order of the interpolating polynomial should be kept low, typically $I_P \leq 5$. The so-called cardinal functions $u_i(x)$ have the property

$$u_i(x_j) = \delta_{ij}, \tag{69}$$

and can be written as

$$u_i(x) = c_i \prod_{\substack{j=1 \\ j \neq i}}^{I_P+1} (x - x_j) = \prod_{\substack{j=1 \\ j \neq i}}^{I_P+1} \frac{x - x_j}{x_i - x_j}, \tag{70}$$

where the normalization factors

$$c_i = \prod_{\substack{j=1 \\ j \neq i}}^{I_P+1} \frac{1}{x_i - x_j}, \tag{71}$$

follow from equation (69). From equation (70), we observe that the cardinal functions $u_i(x)$ depend on x_i, but not on $g(x_i)$. When x_i is on a regular grid, the normalization factors c_i can be precomputed and reused. A polynomial approximation to the derivatives $\partial_x g(x)$ and $\partial_x^2 g(x)$ can be computed in two ways: Equations (68) and (70) can be used directly if $\partial_x g(x_i)$ and $\partial_x^2 g(x_i)$ are available. Otherwise, $\partial_x g(x)$ and $\partial_x^2 g(x)$ can be estimated by differentiation of the interpolating polynomial. In the latter case we obtain

$$\partial_x g(x) \simeq \partial_x P(x) = \sum_{i=1}^{I_P+1} g(x_i)\partial_x u_i(x) \tag{72}$$

$$\partial_x^2 g(x) \simeq \partial_x^2 P(x) \quad = \quad \sum_{i=1}^{I_P+1} g(x_i) \partial_x^2 u_i(x) \tag{73}$$

where the derivatives of the cardinal functions are given by

$$\partial_x u_i(x) \quad = \quad c_i \sum_{\substack{j=1 \\ j \neq i}}^{I_P+1} \prod_{\substack{k=1 \\ k \neq i,j}}^{I_P+1} (x - x_k) \tag{74}$$

$$\partial_x^2 u_i(x) \quad = \quad c_i \sum_{\substack{j=1 \\ j \neq i}}^{I_P+1} \sum_{\substack{k=1 \\ k \neq i,j}}^{I_P+1} \prod_{\substack{l=1 \\ l \neq i,j,k}}^{I_P+1} (x - x_l) \tag{75}$$

Note that if the order of the interpolating polynomial is I_P for $g(x)$, it is $I_P - 1$ for $\partial_x g(x)$ and $I_P - 2$ for $\partial_x^2 g(x)$

Next, we consider 3-D polynomial interpolation on Lagrange form. Let $g(x_i, y_j, z_k)$ denote the value of a discretized function at grid node $(x_i, y_j, z_k) = ((i-1)\Delta x, (j-1)\Delta y, (k-1)\Delta z)$. For our purpose, $g(x_i, y_j, z_k)$ represents one of the elements of the elastic Hooke's tensor c_{ijkl} on a regular grid. The interpolated function $g(x, y, z)$ at the general position $\boldsymbol{x} = (x, y, z)$ can be written as

$$g(x,y,z) \simeq P(x,y,z) = \sum_{i=1}^{I_P+1} \sum_{j=1}^{J_P+1} \sum_{k=1}^{K_P+1} g(x_i, y_j, z_k) u_i(x) v_j(y) w_k(z), \tag{76}$$

where $P(x, y, z)$ is the 3-D interpolating polynomial on Lagrange form,$u_i(x)$ is again given by equation (70) and $v_j(y)$ and $w_k(z)$ are correspondingly obtained from equation (70) by substitution of y and z for x, respectively. The cardinal functions have the property

$$u_i(x_l) v_j(y_m) w_k(z_n) = \delta_{il} \delta_{jm} \delta_{kn}. \tag{77}$$

The order of the interpolating polynomial is controlled by independent parameters I_P, J_P and K_P for each of the Cartesian coordinates. In practice they are often equal. Using equations (72) to (75), we compute the polynomial approximations to the derivatives of $g(x, y, z)$ which can be written as

$$\partial_x g(x,y,z) \simeq \partial_x P(x,y,z) \quad = \quad \sum_{i=1}^{I_P+1} \sum_{j=1}^{J_P+1} \sum_{k=1}^{K_P+1} g(x_i, y_j, z_k) \partial_x u_i(x) v_j(y) w_k(z), \tag{78}$$

$$\partial_x^2 g(x,y,z) \simeq \partial_x^2 P(x,y,z) \quad = \quad \sum_{i=1}^{I_P+1} \sum_{j=1}^{J_P+1} \sum_{k=1}^{K_P+1} g(x_i, y_j, z_k) \partial_x^2 u_i(x) v_j(y) w_k(z), \tag{79}$$

$$\partial_x \partial_y g(x,y,z) \simeq \partial_x \partial_y P(x,y,z) \quad = \quad \sum_{i=1}^{I_P+1} \sum_{j=1}^{J_P+1} \sum_{k=1}^{K_P+1} g(x_i, y_j, z_k) \partial_x u_i(x) \partial_y v_j(y) w_k(z), \tag{80}$$

$$\vdots$$

and so on.

Figures 16 - 18 show a numerical example where we compare ray-tracing results obtained with analytical and gridded representations of the 3-D Gaussian-lens model. The grid spacing is $\Delta x = \Delta y = \Delta z = 10.0$ m. For traveltime (Figure 16) and slowness (Figure 17), the results obtained with the gridded model is very accurate when third-order interpolating polynomials, i.e. $I_P = J_P = K_P = 3$ are used. The geometrical spreading (Figure 18) depends on the second derivatives of the elastic moduli. The accuracy of the geometrical spreading is improved by increasing the order of the polynomial to $I_P = J_P = K_P = 5$, which corresponds to a third-order polynomial approximation to the second-derivatives of the Hookse's tensor.

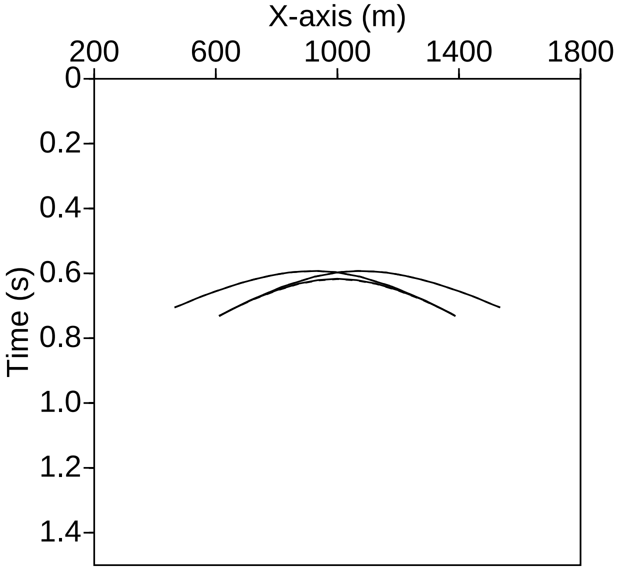

Figure 16: Traveltimes at depth $z = 900$ m. 3-D Gaussian model. Gridded model (solid) and analytical model (dotted). The order of the interpolating polynomial is $I_P = J_P = K_P = 3$

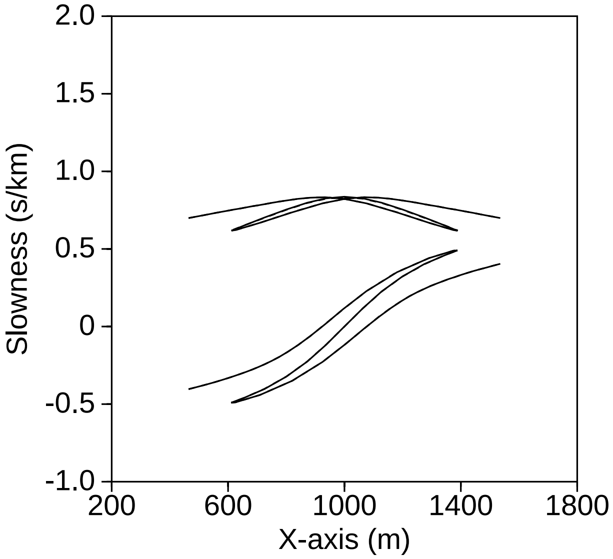

Figure 17: Slowness x- and z-components at depth $z = 900$ m. 3-D Gaussian model. Gridded model (solid) and analytical model (dotted). The order of the interpolating polynomial is $I_P = J_P = K_P = 3$

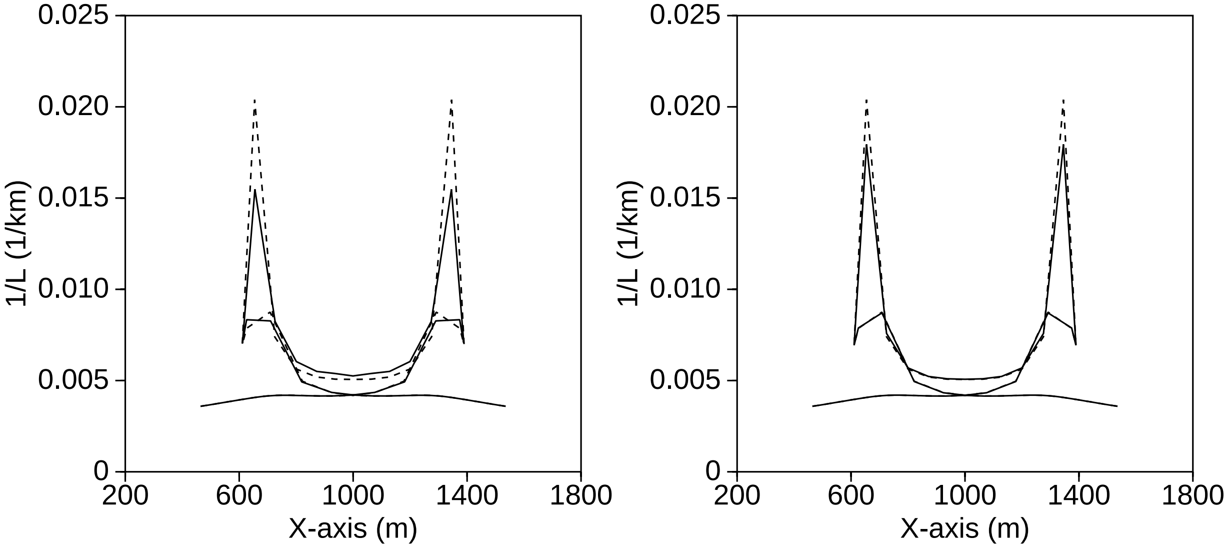

Figure 18: Relative geometrical spreading at depth $z = 900$ m. 3-D Gaussian model. Gridded model (solid) and analytical model (dotted). The order of the interpolating polynomial is $I_P = J_P = K_P = 3$ (left) and $I_P = J_P = K_P = 5$ (right).

N_{CPU}	T_N (sec)	T_C (sec)	S_{rel}	E_{rel}
1	602	584	1.00	1.00
2	254	479	2.37	1.19
4	141	502	4.26	1.07
8	103	693	5.84	0.73
16	78	984	7.71	0.48
32	88	2278	6.84	0.21

Table 2: Elapsed time T_N, CPU time T_C, relative speedup S_{rel} and efficiency E_{rel} for initial-value ray tracing of 2791 rays and interpolation of ray data on a regular 3-D grid. Measured times are given in seconds. The computations were performed on a Silicon Graphics Origin 2000.

4 Computational cost

The anisotropic elastic initial-value ray tracer was implemented and tested on a Silicon Graphics Power Challenge. The software has been designed for the hardware and parallel-processing model used in this computer, so-called symmetrical multiprocessing (SMP). This parallel-processing model is based on a shared-memory architecture, such that all processors share a common address space. The ray tracer is parallelized on a relatively high level. On a computer with N_{CPU} processors, N_{CPU} rays are traces simultaneously and independently.

We studied the computational efficiency of the ray tracer by initial-value ray tracing and interpolation of the ray data to a 3-D grid for one shot position. We traced 2791 rays with 101 timesteps for each ray. The elapsed time T_N, CPU time T_C, relative speedup S_{rel} and efficiency E_{rel} is given in Table 2. The relative speedup and efficiency is shown graphically in Figure 19. The superlinear speedup for $N_{CPU} = 2$ is probably a cache effect. For $N_{CPU} = 16$, the elapsed time is 78 s, which corresponds to approximately 1100 shots, or equivalently 3 million rays, per day.

Profiling of the code reveals that a major part of the computational effort is the interpolation of the

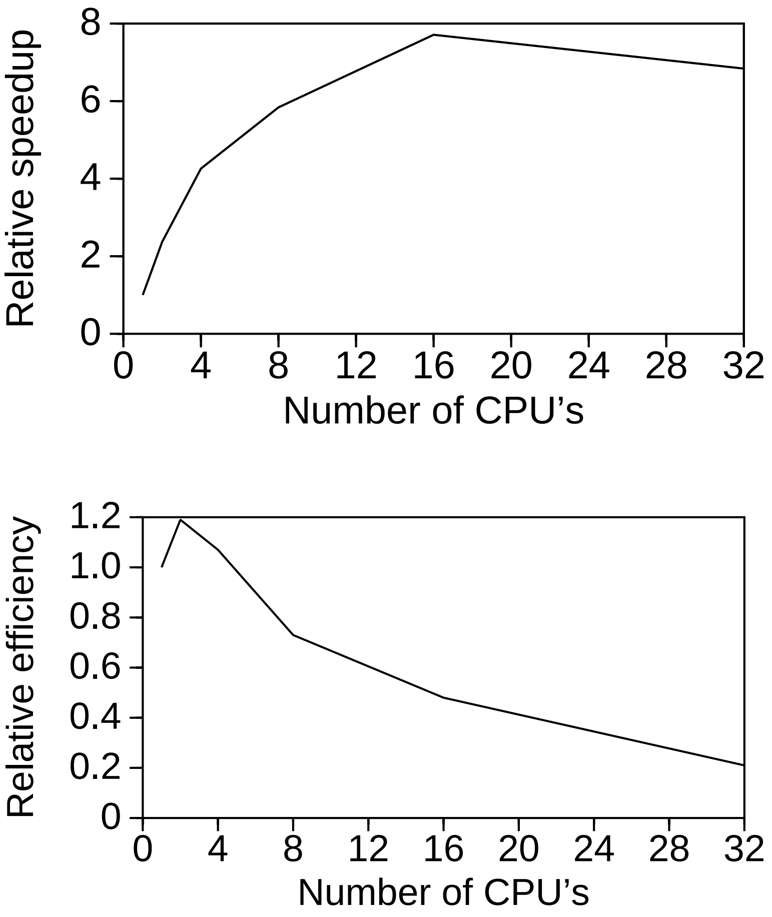

Figure 19: Relative speedup (top) and efficiency (bottom) for initial-value ray tracing of 2791 rays and interpolation of ray data on a regular 3-D grid. The computations were performed on a Silicon Graphics Origin 2000.

geological model, because of the large number of multiplications and additions involved in the 3-D polynomial interpolation. Hence, the best numerical performance is obtained with low-order interpolating polynomials.

5 Discussion and conclusions

We have presented the theoretical background and numerical implementation of a 3-D anisotropic elastic initial ray tracer. The numerical integration of the kinetic and dynamic ray tracing systems is performed by the fifth-order Runge-Kutta method. The main limitation of the present implementation is that shear wave anisotropy need to be present. In isotropic media and some symmetry direction in anisotropic media, the S-wave velocities are degenerate. For these special cases, special routines that are selected automatically in conditional branches should be implemented. For P-waves these problems do not occur.

The initial-value ray tracer has been designed to run in parallel on a shared-memory multiprocessor computer. Several independent rays, corresponding to different initial polar and azimuth angles, are traced concurrently.

The geological model is represented on a regular grid. This provides a simple and generally applicable representation of the medium, such that the same grid can be applied for ray tracing and finite difference modeling. In general, the ray trajectories does not coincide with the nodes of the grid, such that interpolation of the medium is required. Polynomial interpolation is applied to obtain the elastic parameters and their spatial derivatives along the rays. The polynomial interpolation of the medium accounts for a significant part of the computational cost. Therefore, the order of the interpolating polynomials should be low (maximum 5, recommended 3).

The initial value ray tracing is performed for a user defined range of initial polar and azimuth angles. 2-D ray tracing can be performed as a special case with only one azimuth direction. In 3-D ray tracing, the number of azimuth directions is increased with increasing initial phase angle, to obtain a uniform ray coverage and reduce the total number of rays. In 2-D and 3-D prestack Kirchhoff migration, rays must be traced downwards from each shot or receiver position. The ray-theoretical quantities of interest (traveltime, geometrical spreading etc) must be interpolated on a regular image grid. The interpolation has been implemented to honor multipathing and wavefront triplications. This may be useful even if the migration scheme does not account for multipathing, because the selection of events can be based on different criteria (minimum traveltime, maximum amplitude) if multipathing exists.

References

[1] Beylkin, G. and Burridge, R., 1990, Linearized inverse scattering problems in acoustics and elasticity, Wave Motion, **12**, 15–52.

[2] Bleistein, N., 1984, Mathematical methods for wave phenomena, Academic Press, Orlando.

[3] Brandsberg-Dahl, S., Hokstad, K., de Hoop, M.V., and Ursin, B., 2000, 3-D Maslov Green's function in inhomogeneous anisotropic elastic media, *in* Workshop meeting on seismic waves in laterally inhomogenous media V, Charles University, Praha.

[4] Červený, V., 1995, Seismic wave fields in three-dimensional isotropic and anisotropic structures, Lecture notes. University of Trondheim.

[5] de Hoop, M.V. and Brandsberg-Dahl, S., Maslov asymptotic extension of Generalized Radon Transform Inversion in anisotropic elastic media: A least-squares approach, Technical Report CWP-297, Center for Wave Phenomena, Colorado School of Mines, 1999.

[6] Goldstein, H., 1980, Classical Mechanics, 2nd Edition, Addison-Wesley Publishing Company.

[7] Hokstad, K., 1999, Elastic imaging of multicomponent seismic data, Ph.D. thesis, The Norwegian University of Science and Technology.

[8] Hokstad, K., 2000, Multicomponent kirchhoff migration, Geophysics, **65**, May/June .

[9] Kendall, J-M. and Thomson, C.J., 1992, Maslow ray summation, pseudo caustics, lagrangian equivalence and transient seismic waveforms, Geophys. J., **94**, 237–247.

[10] Kincaid, D and Cheney, W., 1991, Numerical analysis, Brooks/Cole Publisher Company.

[11] Press, W.H., Teukolsky, A.S., Vetterling, W.T., and Flannery, B.P., 1992, Numerical Receipes in Fortran, Cambridge University Presss.

[12] Schleicher, J., Tygel, M., and Hubral, P., 1993, 3-D true-amplitude finite offset migration, Geophysics, **58**, 1112–1126.

[13] Vinje, V., Iversen, E., and Gjøystdal, H., 1993, Traveltime and amplitude estimation using wavefront construction, Geophysics, **58**, 1157–1166.

[14] Wang, L. and Belistein, N., 1998, 3-D multi-valued traveltime and amplitude maps, *in* 68th Internat. Mtg., Soc. Expl. Geophys., Expanded Abstracts, 1879–1882.

[15] Xu, S., Chauris, H., Lambré, G., and Noble, M., 1998, Common angle image gather: A strategy for imaging complex media, *in* Expanded Abstracts, 1538–1541, Soc. Expl. Geophys.